

Metal active sites regulation in copper phthalocyanine/bismuth vanadate Z-scheme heterojunction by electron-withdrawing substituent for selective CO₂ photoreduction in pure water

Zichun He ¹, Ye Liu ¹, Zhuo Li, Shuai Xu, Zhijun Li, Ji Bian ^{*}, Liqiang Jing ^{*}

Key Laboratory of Functional Inorganic Materials Chemistry (Ministry of Education), School of Chemistry and Materials Science, International Joint Research Center and Lab for Catalytic Technology, Heilongjiang University, Harbin 150080, PR China

ARTICLE INFO

Keywords:

Bismuth vanadate
Electron-withdrawing substituent grafting
M-N₄ site regulation
Z-scheme heterojunction
CO₂ conversion

ABSTRACT

Here, a Z-scheme heterojunction photocatalyst by integration of copper phthalocyanine with carboxyl grafting (CuTcPc) and BiVO₄ nanosheets (BVO) via the hydroxyl induced assembly strategy has been developed for selective CO₂ photoreduction. The optimal CuTcPc/BVO catalyst delivers a 21-fold increments in CO yields compared with pristine BVO and 91 % selectivity towards CO₂ reduction, coupled with nearly stoichiometric O₂ in pure water. As unraveled by experimental results and theoretical simulations, the remarkably improved photoactivity is attributed to the complementary light absorption of BVO and CuTcPc, the enhanced charge transfer and separation due to the formation of Z-scheme heterojunction and most importantly the preferable CO₂ adsorption and activation brought by the adjusted local coordination and electronic environment of central Cu-N₄ sites by electron-withdrawing substituents. This study provides a feasible avenue to manipulate the active sites from the perspective of functional substitute tailoring on metal phthalocyanine over novel BiVO₄-based Z-scheme heterojunctions for artificial photosynthesis.

1. Introduction

Transforming CO₂ into solar fuels and value-added chemicals by sustainable techniques *eg.* photocatalysis is one of the most promising avenues to mitigate the excessive emission of CO₂ and contribute carbon neutrality [1–3]. The exploitation of efficient catalysts is the key to access photocatalytic CO₂ reduction reaction (CO₂RR) [4]. Constructing artificial Z-scheme heterojunctions by mimicking natural photosynthesis is viable, since the function of the employed two constituents (oxidative photocatalyst, OP and reductive photocatalyst, RP) well matches the natural ones [5,6], namely, electrons induced CO₂ reduction to carbohydrate and photoholes initiated water oxidation to O₂. Therefore, selecting rational OP and RP with sufficient thermodynamical energy is the primary consideration for building such a Z-scheme heterojunction.

Bismuth vanadate (BiVO₄) has been an ideal candidate for the OP benefitting from the merits of narrow bandgap, chemical stability and most importantly the benign water oxidation properties [7–9], which is conducive to the sluggish half-reaction of the water involved CO₂RR.

Hence, seeking an appropriate reduction counterpart with negative conduction band (CB) to integrate with BiVO₄ is of great significance. Even some successful examples of BiVO₄-based Z-scheme heterojunctions have been explored in recent years, the photocatalytic activity is still hindered by the limited optical absorption, sluggish charge separation and the insufficient catalytic active sites [10,11]. In this regard, developing novel RP with wide visible light response and endowed with preferable CO₂ activation centers is an imperative pathway. Aimed to these objectives, metal phthalocyanine (MPC) had been evidenced as an adorable RP for photocatalysis since the complementary optical absorption range, the negative enough CB and the well-defined isolated M-N₄ catalytic active centers [12–14]. However, the photocatalytic activity of CO₂RR is still inferior caused by the moderate CO₂ adsorption and activation at the bare M-N₄ sites, and the inherent electronic structure makes it challenging to break the linear relationship between the catalytic activity and the adsorption energy of reaction intermediates [15–17]. In this sense, to manipulate the electron structure of the center metal is a feasible avenue to regulate the catalytic capacities and hence to improve the photocatalytic activities.

* Corresponding authors.

E-mail addresses: bianji@hlju.edu.cn (J. Bian), jinglq@hlju.edu.cn (L. Jing).

¹ Z. He and Y. Liu contributed equally to this work.



The molecular structure flexibility of MPC enables optimal catalytic properties by connecting the electron withdrawing or donating periphery substituents to adjust the local coordination and electronic environment of M-N₄ center [18–20]. Introduction of electron withdrawing ligand (eg. -CN group, fluorine group, etc.) to MPC macro-cycle has been evidenced to remarkably improve the CO₂RR in electrocatalysis [21,22], yet the influence of peripheral ligand of substituents on the catalytic behaviors of active sites (M-N₄) for photocatalysis has rarely been reported, especially in such a Z-scheme heterojunction. In addition, the dispersion of the employed MPC in solution and the interactions between MPC and inorganic BiVO₄ are also among the vital considerations, since it is closely related to the controllable assembly of MPC on BiVO₄ and hence the exposed available M-N₄ sites density for photocatalytic CO₂RR.

As a proof of concept, copper phthalocyanine with carboxyl grafting (CuTcPc) is applied to integrate with BiVO₄ for building the Z-scheme heterojunction towards photocatalytic CO₂RR. The carboxyl group was functionalized onto CuPc in attempt to regulate the local coordination and electronic environments of Cu-N₄ centers, and potentially manipulate the assembly procedure benefitting from the preferable solubility. As a result, the optimal catalyst delivers a 42 μmol g⁻¹ h⁻¹ CO₂ to CO generation rate with 91 % selectivity, coupled with nearly stoichiometric O₂ in pure water without any sacrificial agent. The improved photocatalytic activity is mainly attributed to the complementary light absorption of BiVO₄ and CuTcPc, the enhanced charge transfer and separation due to the formation of Z-scheme heterojunction and most importantly the preferable CO₂ adsorption and activation, as revealed by series of *in-situ/ex* spectroscopies and theoretical simulations. This study provides insight into the precise modulation of active sites on MPC at the molecular level and afford a feasible route for the design of BiVO₄-based Z-scheme heterojunction for artificial photosynthesis.

2. Experimental section

2.1. Synthesis of materials

2.1.1. Synthesis of BiVO₄ (BVO)

In a typical synthesis, 2.21 g of BiCl₃ and 1.05 g of cetyltrimethylammonium bromide (CTAB) were dissolved in 30 mL of ethylene glycol, respectively. Then, the above solutions were mixed together and vigorously stirred for 40 min. After that, 2.80 g of NaVO₃ was added to the mixture and stirred for 20 min. Subsequently, the obtained suspension was transferred to a 100 mL Teflon-lined autoclave and heated at 120 °C for 12 h in an oven. After cooling down to room temperature naturally, the resulting products were washed with ethanol and deionized water and then dried at 60 °C in a vacuum oven. Finally, the obtained sample was calcined at 450 °C for 8 min in a muffle furnace and denoted as BVO.

2.1.2. Synthesis of CuTcPc

The CuTcPc was synthesized following a prior reported method [23]. In a typical synthesis, 4-carboxyphthalic anhydride (CPA) (6.725 g, 35 mmol), urea (12.15 g, 0.2 mol), CuCl₂ (1.175 g, 8.75 mmol), NH₄Cl (0.94 g, 17.5 mmol) and (NH₄)₂Mo₂O₇ (0.107 g, 0.087 mmol) were mixed and thoroughly ground, followed by calcined at 220 °C for 6 h in a muffle furnace. After cooling down to room temperature naturally, the obtained dark powder was soaked with HCl (1 mol L⁻¹) and NaOH (1 mol L⁻¹) solution for 8 h in turn. Then the tetraamido copper phthalocyanine (CuPc-CONH₂) was obtained. The CuPc-CONH₂ was boiled in saturated NaCl solution containing 2 mol L⁻¹ NaOH solution (100 mL) for 6 h in a three-necked bottle. The pH value of the filtrate was adjusted to about 2.0 with concentrated HCl solution. After standing for overnight, the solid was washed with deionized water and methanol many times to obtain the final blue CuTcPc.

2.1.3. Synthesis of CuTcPc/BVO

The CuTcPc modified BVO (CuTcPc/BVO) were fabricated by a hydroxyl induced assembly strategy. Specifically, the as-prepared BVO (0.1 g) were introduced in 60 mL ethanol and sonicated for 30 min. In parallel, a desired volume of CuTcPc ethanol dispersion was added into the BVO suspension and sonicated for 1 h. Subsequently, the suspension was further stirred at room temperature for 24 h and then evaporated under vigorous stirring at 80 °C. The obtained solid was dried overnight at 80 °C and denoted as xCuTcPc/BVO, where x % indicates the feeding mass percentage (1, 1.5 and 2 %) of CuTcPc to BVO. In particular, 1.5CuTcPc/BVO is denoted as CuTcPc/BVO for short. CuPc modified BVO (CuPc/BVO) was synthesized as the reference by an identical method but replace CuTcPc with commercial CuPc.

2.2. Characterization methods

The detailed characterizations can be found in [Supporting Information \(SI\)](#).

2.3. Evaluation of photocatalytic activities for CO₂ conversion

The photocatalytic reaction was conducted on a 100 mL quartz cell reactor equipped with a 300 W Xenon lamp as the light source. The as-prepared catalyst (20 mg) was suspended in 10 mL of water under magnetic stirring. High-purity CO₂ (99.999 %) gas was passed through water and then introduced into the reaction setup to reach ambient pressure. The photocatalyst was allowed to equilibrate in the CO₂/H₂O system for 30 min and followed by UV-vis light irradiation for 2 h. During irradiation, 0.25 mL of gas produced was taken from the reaction cell at given time intervals for reduction products concentration analysis using a gas chromatograph (GC-7920 with both TCD and FID detectors, Au Light, Beijing). The isotope-labeled experiment was carried out using ¹³CO₂ instead of ¹²CO₂, and the reduction products were analyzed on a gas chromatography-mass spectrometry (GC-MS, MS5977A, Agilent). The product selectivity was calculated according to the following equation:

$$\text{CO selectivity} = \frac{2 \times Y(\text{CO})}{2 \times Y(\text{CO}) + 8 \times Y(\text{CH}_4)}$$

where Y(CO) and Y(CH₄) represent the yield (production rate) of CO and CH₄, respectively.

3. Results and discussion

3.1. Structural characterization

CuTcPc/BVO heterojunctions are constructed by a hydroxyl-induced assembly strategy ([Fig. S1](#)). The carboxyl-functionalized copper phthalocyanine (CuTcPc) is synthesized through the solid-state polymerization method with 4-carboxyphthalic anhydride (CPA) and CuCl₂ as raw materials. Thereafter, the as-fabricated CuTcPc is introduced in ethanol to assemble with BVO to access the heterojunction construction. CuPc modified BVO (CuPc/BVO) has also been prepared in a similar way with commercial CuPc without carboxyl substituent as a reference.

The molecular structure of the as-fabricated CuTcPc was characterized by series of spectroscopies. As revealed by Raman spectra ([Fig. S2](#)), the characteristic bands at 681 and 745 cm⁻¹ are associated with the breathing and deformation of C-C bonds in the macrocycle of CuTcPc. Meanwhile, the typical isoindole ring stretching and the metal ions interaction with the phthalocyanine ring are also recorded at 1445 and 1545 cm⁻¹, respectively [24]. The skeleton feature of CuTcPc was further ascertained by Fourier transform infrared spectroscopy (FT-IR) with the collected vibration peaks at 750, 942, 1297, 1538 and 1606 cm⁻¹ ([Fig. S3](#)). Importantly, the signals at 1119, 1735 and 3300–3543 cm⁻¹ that assigned to the breathing and deformation of the C-O, C=O bonds and the stretching vibration of the O-H bond [25] could also be observed, providing clear evidence for the carboxyl groups.

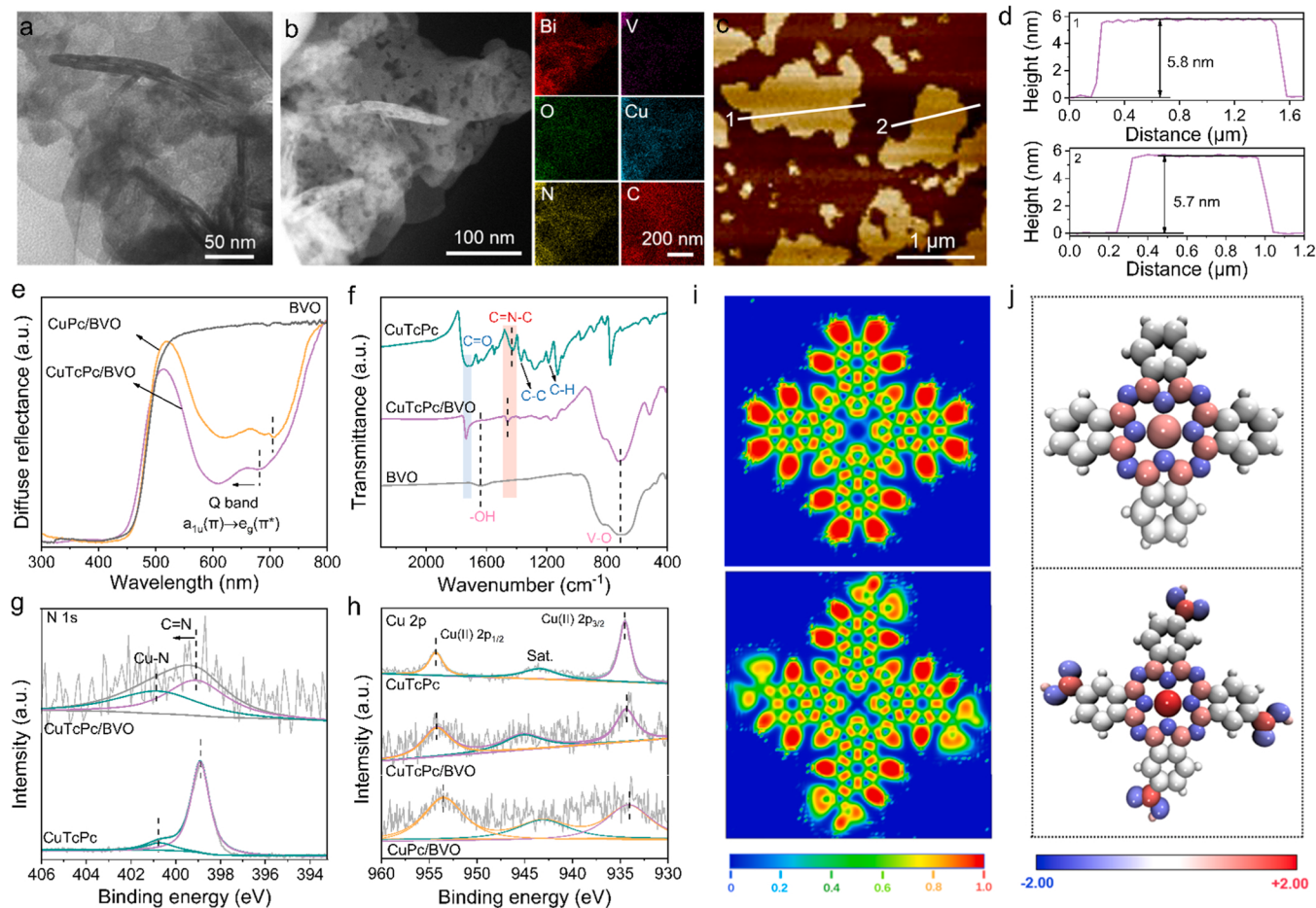


Fig. 1. (a) TEM image, (b) HAADF image of CuTcPc/BVO and the corresponding EDX mapping images of elemental Bi, V, O, Cu, N and C. (c, d) AFM image and the corresponding height profiles of CuTcPc/BVO. (e) UV-vis diffuse reflection spectra of CuTcPc/BVO, CuPc/BVO and BVO. (f) FT-IR spectra of CuTcPc, CuTcPc/BVO and BVO. (g) XPS analyses for N 1s of CuTcPc and CuTcPc/BVO. (h) XPS analyses for Cu 2p of CuTcPc/BVO, CuTcPc and CuPc/BVO. (i) Electron localization function (ELF) mapping of CuPc (top) and CuTcPc (bottom). The ELF function can range from 0 to 1. ELF=1 corresponds to perfect localization, while ELF=0 corresponds to perfect delocalization. (j) Bader charge analysis of CuPc and CuTcPc, respectively. All uncharged atoms are in gray, while blue and red colors indicate the electron accumulation or loss.

Moreover, the chemical structure of the CuTcPc was verified as the molecular ion at ($m/z=751.98$) is recorded by matrix-assisted laser desorption/ionization time of flight mass spectrometry (MALDI-TOF MS) (Fig. S4) [26]. Thereafter, X-ray photoelectron spectroscopy (XPS) was conducted to investigate the chemical states of CuTcPc. The C 1 s spectrum can be deconvoluted to three peaks that attributed to C-C/C=C (284.7 eV), C-N (285.9 eV), and $\pi-\pi^*$ satellite (288.7 eV), respectively (Fig. S5) [27]. As depicted in Fig. S6, the N 1 s XPS displays two peaks at 400.6 and 398.5 eV, corresponding to metal-coordinated nitrogen and pyridinic nitrogen of phthalocyanine ring [28]. Besides, the Cu center in CuTcPc is uncovered to be Cu (II) (Fig. S7). The above indications collectively confirm the successful synthesis of CuTcPc.

The detected characteristic diffraction peaks of BVO match well with the monoclinic phase (JCPDS No. 14-0688) as ascertained by X-ray powder diffraction (XRD) [29]. No noticeable peaks attributed to CuTcPc and CuPc can be observed over the CuTcPc/BVO and CuPc/BVO heterojunctions (Fig. S8), which might be related to the low contents of the loaded phthalocyanines. One can see the morphology character of CuTcPc/BVO (Fig. 1a) has barely changed in comparison with pristine BVO but an amorphous covering as revealed by transmission electron microscopy (TEM) image (Fig. S9). While the evenly dispersion of Bi, V, O, C, N and Cu elements is clearly resolved over CuTcPc/BVO by the corresponding energy dispersive X-ray (EDX) element mappings (Fig. 1b), demonstrating the successful integration of BVO and modified CuTcPc. By comparison, more heavier covering on the surface of BVO is

observed on CuPc/BVO one (the same loading as that of CuTcPc), hinting the carboxyl grafting benefit for the dispersion of CuTcPc (Fig. S10). The average thickness of the CuTcPc/BVO is determined to be 5.8 nm by the AFM image and the corresponding height profiles (Figs. 1c and 1d), with a 1.2 nm increase compared with pristine BVO (Fig. S11), suggesting the stacked CuTcPc on BVO is no more than 3 layers based on the interlayer distance within the planar of MPC as reported earlier [30]. In parallel, it is noticed that the thickness of CuPc/BVO (7.7 nm) is much thicker than that of CuTcPc modified one (Fig. S12), which is consistent with the TEM results. As depicted in Fig. 1e, an additional absorption bands at 600–800 nm appears on CuTcPc/BVO in comparison to pristine BVO, which is assigned to the Q-band absorption of CuTcPc caused by the $a_{1u}(\pi)-e_g(\pi^*)$ transition from the highest occupied molecular orbital (HOMO) to the lowest unoccupied molecular orbital (LUMO) [31]. Apparently, the visible light absorption range is extended with CuTcPc modification. It is worth noting that a blue-shift in the Q band absorption of CuTcPc is observed in comparison with CuPc/BVO one, which is closely related to the introduction of electron-withdrawing substituent. This finding is consistent with the results on individual CuTcPc and CuPc ones that uncovered by ultraviolet-visible (UV-vis) absorption spectra in N, N-dimethylformamide (DMF) (Fig. S13).

FT-IR spectra were conducted to explore the interfacial interactions between CuTcPc and BVO. As shown in Fig. 1f, the vibrations of phthalocyanine ring and center metal-ligand interaction are detected on

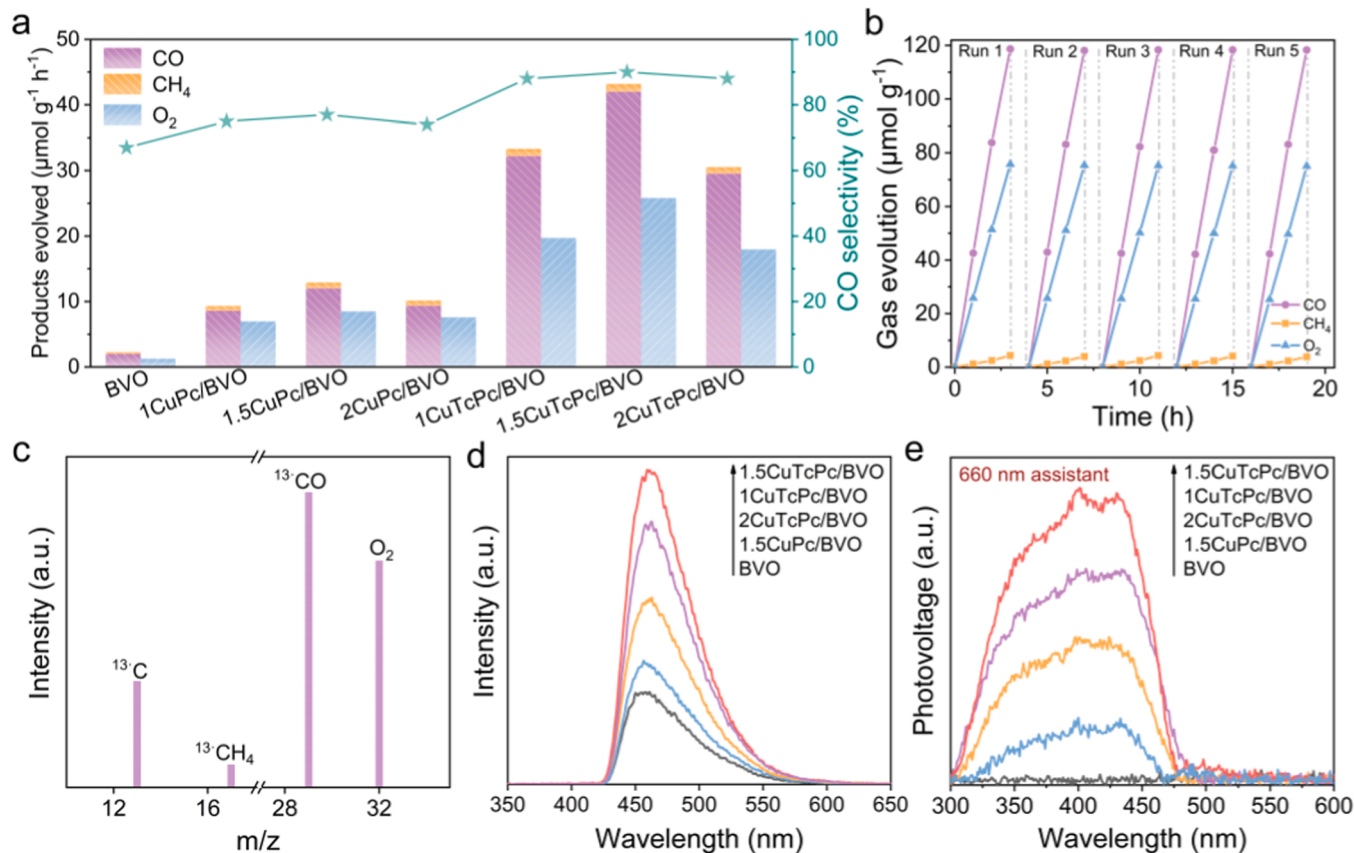


Fig. 2. (a) Photocatalytic activities for CO_2 reduction of $x\text{CuTcPc}/\text{BVO}$, $y\text{CuPc}/\text{BVO}$ and BVO (x and y represent the feeding mass percentage of CuTcPc and CuPc to BVO, respectively). (b) Detected redox products during five consecutive runs of CO_2 reduction over $1.5\text{CuTcPc}/\text{BVO}$ under light irradiation. (c) Mass spectra of the products from the photocatalytic reduction of $^{13}\text{CO}_2$ over $1.5\text{CuTcPc}/\text{BVO}$. (d) Fluorescence spectra related to the formed hydroxyl radicals of $x\text{CuTcPc}/\text{BVO}$, $1.5\text{CuPc}/\text{BVO}$ and BVO. (e) SPS responses of $x\text{CuTcPc}/\text{BVO}$, $1.5\text{CuPc}/\text{BVO}$ and BVO assisted with a 660 nm monochromatic beam.

the CuTcPc/BVO heterojunctions. It is noticed that the $\text{C}=\text{N}-\text{C}$ (1425 cm^{-1}) of CuTcPc exhibits an obvious shift after integration with BVO. In addition, the intensity of surface hydroxyl vibrations for BVO (1640 cm^{-1}) is weakened as the introduction of CuTcPc [25,32]. Moreover, a slight Raman shift for V-O bonds of BVO is observed after CuTcPc modification (Fig. S14). On the basis of the above indication, it is hypothesized that CuTcPc interacts with the V-O bond through the hydroxyl groups on BVO. One can notice that the BE of both Bi 4 f and V 2p for CuTcPc/BVO show a negative shift compared with that of pristine BVO (Fig. S15 and Fig. S16), indicating the electrons of CuTcPc prone to diffuse towards BVO when they come into close contact. On the contrary, a positive BE shift of N 1 s is observed on CuTcPc/BVO in contrast to CuTcPc, while the BE of Cu 2p retains in this case (Fig. 1g and Fig. 1h), suggesting CuTcPc plausibly links with BVO through the ligand N atoms by hydrogen bonding interactions. Moreover, the chemical state of Cu in CuTcPc/BVO is revealed to be Cu (II) as the detected XPS peaks of Cu 2p_{3/2} and Cu 2p_{1/2} are located at around 934.4 and 954.2 eV [33]. One can see the chemical environment of Cu over CuTcPc/BVO is identical to that of CuTcPc. While it delivers a positive shift compared with that of CuPc/BVO one, which plausibly due to the introduction of carboxyl substituents that caused more electrons in the Cu center transfer to the coordinated N atoms [27]. It is in line with the XPS results on pristine CuPc and CuTcPc. This point is further supported by the density functional theory (DFT) calculations. As depicted in Fig. 1i, the mapping of the electron localization function (ELF) shows that the charge delocalization on central Cu is more pronounced after carboxyl substituents modification. Moreover, Bader charge analysis (all uncharged atoms are in gray, while blue and red colors indicate the electron accumulation or loss) (Fig. 1j) indicates that the Cu on CuTcPc is more positively charged

in comparison to CuPc, suggesting the electron can be delocalized on the Cu site by electron withdrawing substituent of carboxyl groups. Apparently, the simulation results are in good agreement with experimental observations.

3.2. Photocatalytic performance of CO_2 reduction and charge separation

The photocatalytic performance of the investigated samples was evaluated by CO_2 reduction in pure water without any sacrificial agent, in which CO and CH_4 are detected as the main reduction products. As shown in Fig. 2a, BVO shows a feeble CO yield of $2.0 \mu\text{mol g}^{-1} \text{ h}^{-1}$, while the yield of CO ascend precipitously as the modification amount of CuTcPc gradually increases. It presents a volcano trend with the optimization of the introduced CuTcPc loadings, in which $1.5\text{CuTcPc}/\text{BVO}$ shows the highest CO generation rate of $42 \mu\text{mol g}^{-1} \text{ h}^{-1}$, delivering 21 times higher than that of BVO. In contrast, even the photocatalytic performance of CuPc/BVO ones with various CuPc loadings is superior to pristine BVO, it far behind that of CuTcPc/BVO heterojunction. Interestingly, it is noticed that the CO selectivity is greatly promoted, in which the optimal $1.5\text{CuTcPc}/\text{BVO}$ reaches up to 91 % in comparison to $1.5\text{CuPc}/\text{BVO}$ (77 %), demonstrating the crucial role of the introduced carboxyl groups on the regulation of photocatalytic activity and selectivity. In parallel, a certain amount of oxidative product O_2 has also been detected.

Moreover, the stability of the as-fabricated catalyst was evaluated across five runs. One can see the photocatalytic activities for $1.5\text{CuTcPc}/\text{BVO}$ and $1.5\text{CuPc}/\text{BVO}$ have no obvious decay after five cycles for CO_2 conversion, indicating the investigated photocatalysts are stable during the reaction (Fig. 2b and Fig. S17). Furthermore, ^{13}C labeled isotopic

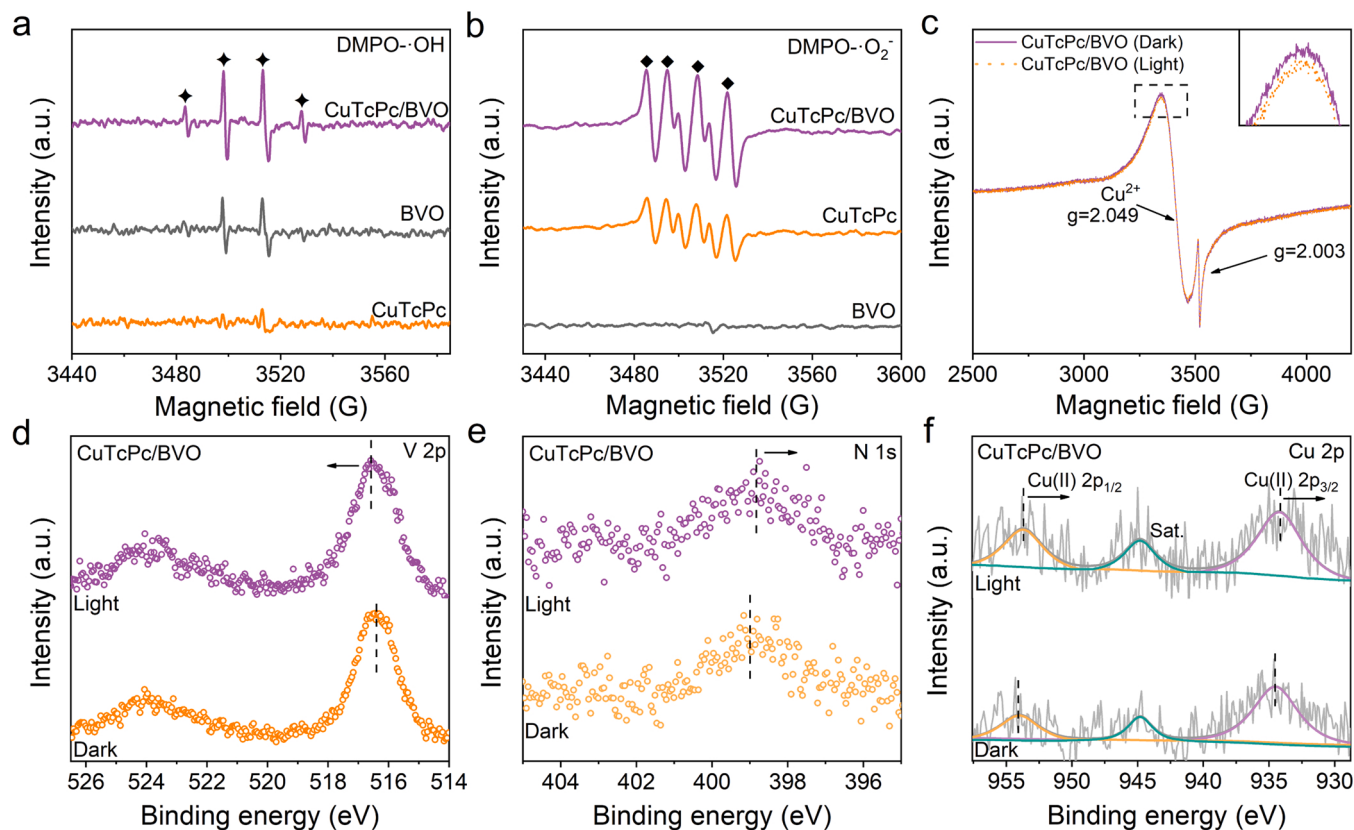


Fig. 3. (a, b) DMPO spin-trapping EPR spectra recorded for $\bullet\text{OH}$ (CuTcPc/BVO, CuTcPc and BVO) and $\bullet\text{O}_2$ (CuTcPc/BVO, CuTcPc and BVO) under light irradiation. The concentration of DMPO is 50 mmol L⁻¹. $\bullet\text{OH}$ and $\bullet\text{O}_2$ were determined in aqueous phase and methanolic solution, respectively. (c) EPR spectra of CuTcPc/BVO in dark and under light irradiation. *In-situ* irradiated XPS analyses for (d) V 2p, (e) N 1s and (f) Cu 2p of CuTcPc/BVO.

experiment was adopted to affirm the carbon source in the reduction products (Fig. 2c). In detail, the peaks at $m/z=29$ and $m/z=17$ are clearly recorded by mass spectra, which can be assigned to ^{13}CO and $^{13}\text{CH}_4$, respectively, indicating the produced CO comes from CO_2 reduction driven by the photocatalysis, rather than the decomposition of CuTcPc.

The charge transfer and separation properties of the typical samples were subsequently investigated by fluorescence (FS) spectra related to the formed hydroxyl radical amounts (Fig. 2d), which is quantified by adding the probe molecule coumarin to generate the luminescent 7-hydroxy coumarin molecules. Higher FS intensity means better charge separation. It can be seen that CuTcPc/BVO ones exhibit stronger FS signals than that of pristine BVO, evidencing the CuTcPc introduction effectively facilitates the charge transfer and separation. Another finding is that all the CuTcPc/BVO heterojunctions deliver better charge separation properties compared to that of 1.5CuPc/BVO, implying carboxyl introduction promotes the charge separation. This is plausibly related to the increased charge carrier density of CuTcPc (Table S1).

The behavior of photogenerated charge carrier was then explored by the steady-state surface photovoltage spectroscopy (SS-SPS), a typical photophysical technique that could reveal the charge separation and recombination by means of the surface potential difference of a semiconductor before and after illumination. In order to rule out the influence of oxygen trapping electrons, the SPS measurement was conducted in a N_2 atmosphere. Considering the selective optical absorption characters of CuTcPc (500–800 nm), an additional 660 nm monochromatic excitation beam was employed as an assistant beam to excite CuTcPc when probing from 300 to 600 nm to guarantee both the CuTcPc and BVO could be excited simultaneously. Electrochemical impedance spectroscopy (EIS) further supports the above results (Fig. S18). A smaller curvature radius represents a lower interfacial resistance, which

is connected with better charge transfer and separation [34]. It can be seen that the 1.5CuTcPc/BVO heterojunction exhibits the smallest curvature radius, indicating the best charge separation. This is consistent with FS and SS-SPS results.

3.3. Mechanism insights

The energy band structures of CuTcPc and BVO were determined by Mott-Schottky (MS) curves. As depicted in Fig. S19 and Fig. S20, the flat band potentials of CuTcPc and BVO are estimated to be 0.45 and -0.3 V versus Ag/AgCl, respectively. In combination of the bandgap energy (E_g) confirmed by DRS spectra, the LUMO levels of CuTcPc and valence band (VB) top of BVO are calculated to be -1.96 and 2.31 V versus NHE, respectively. It is noticed that the estimated LUMO levels of CuTcPc is a more negative than that of CuPc (Fig. S21), which is more favorable for photocatalytic CO_2 reduction. The illustration of the energy band structures of the fabricated BVO, CuTcPc and CuPc is presented in Fig. S22. It can be seen that the energy band alignments of BVO and CuTcPc meet the requirement of Z-scheme heterojunction, and such a charge transfer pathway is theoretically feasible. Electron paramagnetic resonance (EPR) spectra were further carried out to reveal the charge transfer manners between BVO and CuTcPc (Figs. 3a and 3b). One can see an observable EPR signal of the DMPO-•OH adduct with an intensity ratio of 1:2:2:1 is recorded on BVO, yet no detectable signal is observed on CuTcPc under light irradiation, which is caused by the HOMO energy level of CuTcPc is more negative than the potential of $\text{H}_2\text{O}/\bullet\text{OH}$ (1.99 V vs. NHE). In parallel, a distinct EPR signal of DMPO-•O₂ adduct with an intensity ratio of 1:1:1:1 is detected on CuTcPc, while it is invisible over BVO. It can be understandable that the CB potential of BVO is more positive than the standard potential of $\text{O}_2/\bullet\text{O}_2^-$ (-0.33 V vs. NHE). Noticeably, both the DMPO-•OH and DMPO-•O₂ signals of CuTcPc/BVO

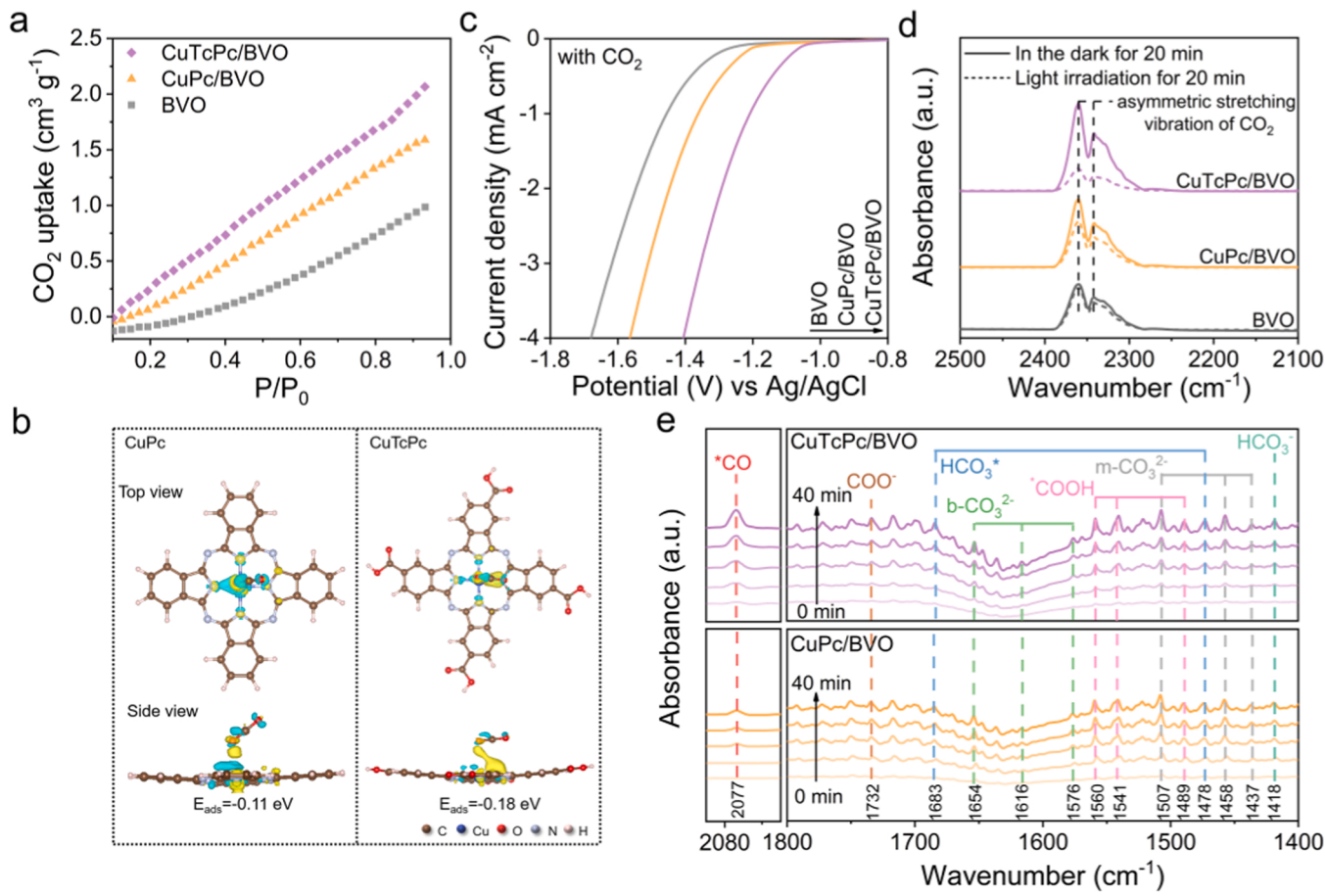


Fig. 4. (a) CO₂ uptake of CuTcPc/BVO, CuPc/BVO and BVO. (b) DFT calculation of optimized geometries and adsorption energies of CO₂ on CuPc (left) and CuTcPc (right), respectively. (c) Electrochemical reduction curves of CuTcPc/BVO, CuPc/BVO and BVO in the CO₂-saturated electrolyte. (d) *In-situ* DRIFTS for adsorbed CO₂ in dark and under light irradiation for 20 min recorded on CuTcPc/BVO, CuPc/BVO and BVO. (e) *In-situ* DRIFTS for the detected intermediates of CuTcPc/BVO (top) and CuPc/BVO (bottom) in course of the light irradiation.

are stronger than those of BVO and CuTcPc, indicating more energetic photogenerated holes and electrons on CuTcPc/BVO are survived to produce •OH and •O₂ radicals by the Z-scheme charge transfer route.

Following the indication of charge transfer manner on CuTcPc/BVO, the subsequent electron transfer is further revealed. As shown in Fig. 3c, two conspicuous EPR signals are observed in CuTcPc/BVO in dark, which are ascribed to Cu²⁺ in CuTcPc ($g=2.049$) and dissociative free electrons ($g=2.003$), respectively [35]. However, the EPR signal of Cu²⁺ is weakened under light irradiation, demonstrating that the central metal accepts the electrons and partially be reduced to Cu⁺ with EPR silence. EPR results strongly support the fact that the coordinated Cu in CuTcPc could further receive the electrons from the ligand following the Z-scheme charge transfer pathway of CuTcPc/BVO. Thereafter, *in-situ* irradiated XPS was performed to further confirm the charge transfer from BVO to CuTcPc. The characteristic peak of N 1 s for CuTcPc/BVO shows a slight shift to lower BE under light irradiation, suggesting an increase of the electron density (Fig. 3e). In contrast, a positive shift for the V 2p is observed, corresponding to a decrease of the electron density on BVO (Fig. 3d). The observed BE variations provide direct evidence for the Z-scheme charge transfer pathway across the CuTcPc/BVO interface, namely, the photoelectrons migrate from BVO to CuTcPc. Moreover, a positive shift of ca. 0.4 eV is recorded for Cu 2p under light irradiation (Fig. 3f), hinting the Cu works as the electron acceptor during the photocatalytic reaction.

To shed light on the mechanism of CO₂ activation and conversion, the CO₂ adsorption capacities of the typical samples were investigated by CO₂ adsorption isotherms (Fig. 4a). Pristine BVO presents inferior

CO₂ adsorption activity to CuTcPc/BVO and CuPc/BVO. As expected, CuTcPc/BVO one exhibits the strongest capacity for CO₂ adsorption. This result is also supported by theoretical simulations. The adsorption energies of CO₂ on the established models of CuPc and CuTcPc were calculated. As shown in Fig. 4b, the adsorption energies of CO₂ on CuPc and CuTcPc are -0.11 and -0.18 eV, respectively, demonstrating the carboxyl grafting promotes the adsorption of CO₂. Furthermore, electrochemical measurements reveal that CuTcPc/BVO delivers the lowest onset potential than that of others in the CO₂-saturated electrolyte, implying its superior ability for CO₂ activation (Fig. 4c). Notably, the onset potential of CuTcPc/BVO in this case is also lower than that in the N₂-saturated electrolyte (Fig. S23), evidencing the CuTcPc/BVO is more beneficial for CO₂ reduction rather than H₂O reduction. Therefore, it can be confirmed that CuTcPc modification is more favorable for CO₂ molecules adsorption and activation in comparison to CuPc one due to the preferable catalytic function after grafting carboxyl functional substitutes.

In-situ diffuse reflectance infrared Fourier transform spectroscopy (DRIFTS) was applied to monitor the intermediates and products involved in the photocatalytic CO₂ conversion process (Fig. 4d and Fig. S24). The absorption bands ranging of 2280–2400 and 3550–3800 cm⁻¹ are attributed to the asymmetric stretching vibration of CO₂ and the surface O-H stretching of H₂O, respectively [36,37]. The CuTcPc/BVO shows the strongest stretching vibration of CO₂ in dark, while the O-H stretching of H₂O recorded on BVO, CuPc/BVO and CuTcPc/BVO are roughly same, implying the introduced CuTcPc is more favorable for CO₂ adsorption rather than water, which is consistent with

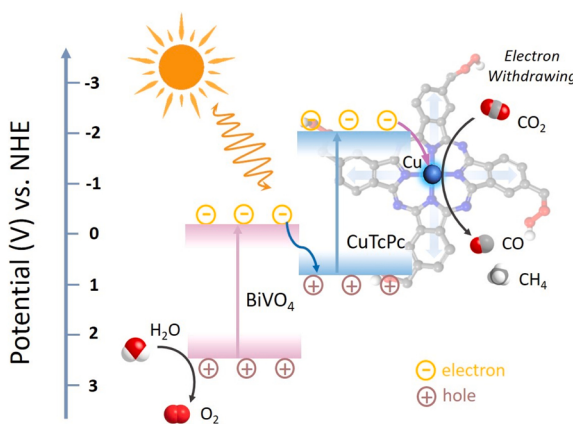


Fig. 5. Mechanism of the proposed Z-scheme charge transfer on CuTcPc/BVO heterojunction and the involved redox reactions.

the results as revealed by CO_2 adsorption isotherms. Under light irradiation, the asymmetric stretching vibration of CO_2 recorded on CuTcPc/BVO is significantly weakened, yet it is not distinct on others. Likewise, the same trends are also observed for O-H stretching under light illumination. The possible intermediates in CO_2 conversion have also been recorded on CuTcPc/BVO under light irradiation, as shown in Fig. 4e. The peaks at 1507, 1458 and 1437 cm^{-1} correspond to monodentate carbonate (m-CO_3^{2-}), while 1654, 1576, 1616 and 1418 cm^{-1} are ascribed to double-ended carbonate (b-CO_3^{2-}) and HCO_3^- , respectively [38,39]. Meanwhile, the signals of COO^- species (1732 cm^{-1}), $^*\text{COOH}$ (1560, 1541 and 1489 cm^{-1}) along with $^*\text{CO}$ (2077 cm^{-1}) gradually emerge with the prolonged irradiation time, implying the evoked CO_2 conversion after its absorption on the active sites. Surprisingly, it can be noticed that the detected dominant intermediates for photocatalytic CO_2 reduction to CO on CuTcPc/BVO increase faster than that of CuPc/BVO during the irradiation intervals, which is believed to be correlated to the carboxyl regulated catalytic capacities on central Cu sites of CuTcPc.

Accordingly, a plausible mechanism of the charge transfer and the involved catalytic process on CuTcPc/BVO is proposed (Fig. 5). The CuTcPc and BVO are excited simultaneously under light irradiation, then the photogenerated electrons migrate from the BVO to CuTcPc following the Z-scheme pathway. Subsequently, the separated electrons on the LUMO of CuTcPc would further transfer from the ligand to the central metal Cu^{2+} to drive CO_2 reduction through the formation of $^*\text{COOH}$ and finally produce CO. On the other hand, the settled holes in the VB of BVO oxidize H_2O to produce O_2 . Notably, the CO selectivity of CuTcPc/BVO would be greatly improved thanks to the introduction of electron-withdrawing substituent.

4. Conclusions

In summary, a Z-scheme heterojunction of CuTcPc/BVO is constructed by the hydroxyl induced assembly strategy for selective CO_2 photoreduction. The optimal 1.5CuTcPc/BVO catalyst delivers a 42 $\mu\text{mol g}^{-1} \text{h}^{-1}$ CO_2 to CO generation rate with 91 % selectivity, which exhibits ca. 3.5-fold and 21-fold increments in CO yields compared with that of CuPc/BVO and pristine BVO, respectively. Experimental results and theoretical simulations reveal that the electronic delocalization at the Cu site is regulated by the carboxyl substitutes, and the adjusted local coordination and electronic environment of the center Cu-N₄ enable preferable CO_2 adsorption and activation. In parallel, the enhanced charge transfer and separation due to the formation of Z-scheme heterojunction as well as the complementary light absorption of BVO and CuTcPc also contribute to the promoted photocatalytic activities for CO_2 RR. This work offers a feasible route to regulate the active sites of MPC in view of ligand tailoring and propose an insight on BiVO₄-based Z-scheme heterojunction design for artificial photosynthesis.

CRediT authorship contribution statement

Liqiang Jing: Writing – review & editing, Visualization, Supervision, Project administration, Funding acquisition. **Ji Bian:** Writing – review & editing, Writing – original draft, Visualization, Validation, Funding acquisition, Conceptualization. **Zhijun Li:** Methodology. **Shuai Xu:** Methodology. **Zhuo Li:** Methodology, Investigation, Formal analysis. **Ye Liu:** Writing – review & editing, Investigation, Formal analysis. **Zichun He:** Writing – original draft, Formal analysis, Data curation.

Declaration of Competing Interest

The authors declare no conflict of interest.

Data availability

Data will be made available on request.

Acknowledgements

This work is financially supported by the National Natural Science Foundation of China (no. U2102211, 22202064, U23A20576), China Postdoctoral Science Foundation (2022M721069), Outstanding Youth Science Foundation of Heilongjiang Province (YQ2023B008) and Postdoctoral Science Foundation of Heilongjiang Province (LBH-Z22034). Z. He and Y. Liu contributed equally to this work.

Appendix A. Supporting information

Supplementary data associated with this article can be found in the online version at doi:10.1016/j.apcatb.2024.124207.

References

- [1] E. Gong, S. Ali, C.B. Hiragond, H.S. Kim, N.S. Powar, D. Kim, H. Kim, S.I. In, Solar fuels: research and development strategies to accelerate photocatalytic CO_2 conversion into hydrocarbon fuels, *Energy Environ. Sci.* 15 (2022) 880–937, <https://doi.org/10.1039/dlee02714j>.
- [2] H. Shang, Y. Chen, S. Guan, Y. Wang, J. Cao, X. Wang, H. Li, Z. Bian, Scalable and selective gold recovery from end-of-life electronics, *Nat. Chem. Eng.* 1 (2024) 170–179, <https://doi.org/10.1038/s44286-023-00026-w>.
- [3] Y. Chen, M. Xu, J. Wen, Y. Wan, Q. Zhao, X. Cao, Y. Ding, Z. Wang, H. Li, Z. Bian, Selective recovery of precious metals through photocatalysis, *Nat. Sustain.* 4 (2021) 618–626, <https://doi.org/10.1038/s41893-021-00697-4>.
- [4] X. Chen, S. Guan, J. Zhou, H. Shang, J. Zhang, F. Lv, H. Yu, H. Li, Z. Bian, Photocatalytic free radical-controlled synthesis of high-performance single-atom catalysts, *Angew. Chem. Int. Ed.* 62 (2023) e202312734, <https://doi.org/10.1002/anie.202312734>.
- [5] Y. Kang, H. Qi, G. Wan, C. Zhen, X. Xu, L. Yin, L. Wang, G. Liu, H. Cheng, Ferroelectric polarization enabled spatially selective adsorption of redox mediators to promote Z-scheme photocatalytic overall water splitting, *Joule* 6 (2022) 1876–1886, <https://doi.org/10.1016/j.joule.2022.06.017>.
- [6] A. Shi, D. Sun, X. Zhang, S. Ji, L. Wang, X. Li, Q. Zhao, X. Niu, Direct Z-scheme photocatalytic system: insights into the formative factors of photogenerated carriers transfer channel from ultrafast dynamics, *ACS Catal.* 12 (2022) 9570–9578, <https://doi.org/10.1021/acscatal.2c01959>.
- [7] Y. Qi, J. Zhang, Y. Kong, Y. Zhao, S. Chen, D. Li, W. Liu, Y. Chen, T. Xie, J. Cui, C. Li, K. Domen, F. Zhang, Unraveling of cocatalysts photodeposited selectively on facets of BiVO₄ to boost solar water splitting, *Nat. Commun.* 13 (2022) 484, <https://doi.org/10.1038/s41467-022-28146-6>.
- [8] S. Liu, R. Gao, R. Zhang, Z. Wang, X. Liu, T. Nakajima, X. Zhang, Y. Su, L. Wang, Tungsten induced defect control on BiVO₄ photoanodes for enhanced solar water splitting performance and photocorrosion resistance, *Appl. Catal. B-Environ.* 298 (2021) 120610, <https://doi.org/10.1016/j.apcatb.2018.04.026>.
- [9] S. Lin, H. Huang, T. Ma, Y. Zhang, Photocatalytic oxygen evolution from water splitting, *Adv. Sci.* 8 (2021) 2002458, <https://doi.org/10.1002/advs.202002458>.
- [10] J. Bian, Z. Zhang, J. Feng, M. Thangamuthu, F. Yang, L. Sun, Z. Li, Y. Qu, D. Tang, Z. Lin, F. Bai, J. Tang, L. Jing, Energy platform for directed charge transfer in the cascade Z-scheme heterojunction: CO_2 photoreduction without a cocatalyst, *Angew. Chem. Int. Ed.* 60 (2021) 20906–20914, <https://doi.org/10.1002/anie.202106929>.
- [11] L. Sun, Z. Zhang, J. Bian, F. Bai, H. Su, Z. Li, J. Xie, R. Xu, J. Sun, L. Bai, C. Chen, Y. Han, J. Tang, L. Jing, A Z-scheme heterojunctional photocatalyst engineered with spatially separated dual redox sites for selective CO_2 reduction with water: insight by in-situ μ -transient absorption spectra, *Adv. Mater.* 35 (2023) 2300064, <https://doi.org/10.1002/adma.202300064>.

- [12] J. Bian, J. Feng, Z. Zhang, Z. Li, Y. Zhang, Y. Liu, S. Ali, Y. Qu, L. Bai, J. Xie, D. Tang, X. Li, F. Bai, J. Tang, L. Jing, Dimension-matched zinc phthalocyanine/BiVO₄ ultrathin nanocomposites for CO₂ reduction as efficient wide-visible-light-driven photocatalysts via a cascade charge transfer, *Angew. Chem. Int. Ed.* 58 (2019), <https://doi.org/10.1002/ange.201905274>, 10764–10764.
- [13] G. Liu, Y. Zhu, H. Gao, S. Xu, Z. Wen, L. Sun, F. Li, Photocatalytic water oxidation by surface modification of BiVO₄ with heterometallic polyphthalocyanine, *ACS Catal.* 13 (2023) 8445–8454, <https://doi.org/10.1021/acscatal.3c01235>.
- [14] J. Feng, J. Bian, L. Bai, S. Xi, Y. Wang, C. Chen, L. Jing, Efficient wide-spectrum photocatalytic overall water splitting over ultrathin molecular nickel phthalocyanine/BiVO₄ Z-scheme heterojunctions without noble metals, *Appl. Catal. B Environ.* 295 (2021) 120260, <https://doi.org/10.1016/j.apcatb.2021.120260>.
- [15] J. Cao, Z. Xu, Y. Chen, S. Li, Y. Jiang, L. Bai, H. Yu, H. Li, Z. Bian, Tailoring the asymmetric structure of NH₂-UiO-66 metal-organic frameworks for light-promoted selective and efficient gold extraction and separation, *Angew. Chem. Int. Ed.* 135 (2023) e202302202, <https://doi.org/10.1002/ange.202302202>.
- [16] X. Zhang, Y. Wang, M. Gu, M. Wang, Z. Zhang, W. Pan, Z. Jiang, H. Zheng, M. Lucero, H. Wang, G.E. Sterbinsky, Q. Ma, Y. Wang, Z. Feng, J. Li, H. Dai, Y. Liang, Molecular engineering of dispersed nickel phthalocyanines on carbon nanotubes for selective CO₂ reduction, *Nat. Energy* 5 (2020) 684–692, <https://doi.org/10.1038/s41560-020-0667-9>.
- [17] Y. Wu, Z. Jiang, X. Lu, Y. Liang, H. Wang, Domino electroreduction of CO₂ to methanol on a molecular catalyst, *Nature* 575 (2019) 639–642, <https://doi.org/10.1038/s41586-019-1760-8>.
- [18] S. Yuan, J. Peng, Y. Zhang, D.J. Zheng, S. Bagi, T. Wang, Y. Román-Leshkov, Y. Shao-Horn, Tuning the catalytic activity of Fe-phthalocyanine-based catalysts for the oxygen reduction reaction by ligand functionalization, *ACS Catal.* 12 (2022) 7278–7287, <https://doi.org/10.1021/acscatal.2c00184>.
- [19] Y. Chen, S. Guan, H. Ge, X. Chen, Z. Xu, Y. Yue, H. Yamashita, H. Yu, H. Li, Z. Bian, Photocatalytic dissolution of precious metals by TiO₂ through photogenerated free radicals, *Angew. Chem. Int. Ed.* 134 (2022) e202213640, <https://doi.org/10.1002/ange.202213640>.
- [20] S. Zhou, L. Zhang, L. Zhu, C. Tung, L. Wu, Amphiphilic cobalt phthalocyanine boosts carbon dioxide reduction, *Adv. Mater.* 35 (2023) 2300923, <https://doi.org/10.1002/adma.202300923>.
- [21] X. Zhang, Z. Wu, X. Zhang, L. Li, Y. Li, H. Xu, X. Li, X. Yu, Z. Zhang, Y. Liang, H. Wang, Highly selective and active CO₂ reduction electrocatalysts based on cobalt phthalocyanine/carbon nanotube hybrid structures, *Nat. Commun.* 8 (2017) 14675, <https://doi.org/10.1038/ncomms14675>.
- [22] J. Su, J. Zhang, J. Chen, Y. Song, L. Huang, M. Zhu, B. Yakobson, B. Tang, R. Ye, Building a stable cationic molecule/electrode interface for highly efficient and durable CO₂ reduction at an industrially relevant current, *Energy Environ. Sci.* 14 (2021) 483–492, <https://doi.org/10.1039/D0EE02535F>.
- [23] B. Shang, F. Zhao, C. Choi, X. Jia, M. Pauly, Y. Wu, Z. Tao, Y. Zhong, N. Harmon, P. A. Maggard, T. Lian, N. Hazari, H. Wang, Monolayer molecular functionalization enabled by acid-base interaction for high-performance photochemical CO₂ reduction, *ACS Energy Lett.* 7 (2022) 2265–2272, <https://doi.org/10.1021/acsenergylett.2c01147>.
- [24] E.A. Moges, C.Y. Chang, W.H. Huang, K. Lakshmanan, Y.A. Awoke, C.W. Pao, M. C. Tsai, W.N. Su, B.J. Hwang, Sustainable synthesis of dual single-atom catalyst of Pd-N₄/Cu-N₄ for partial oxidation of ethylene glycol, *Adv. Funct. Mater.* 32 (2022) 2206887, <https://doi.org/10.1002/adfm.202206887>.
- [25] K.S. Song, P.W. Fritz, D.F. Abbott, L.N. Poon, C.M. Caridade, F. Gándara, V. Mougel, A. Coskun, Mixed-metal ionothermal synthesis of metallophthalocyanine covalent organic frameworks for CO₂ capture and conversion, *Angew. Chem. Int. Ed.* 62 (2023) e202309775, <https://doi.org/10.1002/anie.202309775>.
- [26] J. Yuan, S. Chen, Y. Zhang, R. Li, J. Zhang, T. Peng, Structural regulation of coupled phthalocyanine-porphyrin covalent organic frameworks to highly active and selective electrocatalytic CO₂ reduction, *Adv. Mater.* 34 (2022) 2203139, <https://doi.org/10.1002/adma.202203139>.
- [27] K. Zhang, J. Xu, T. Yan, L. Jia, J. Zhang, C. Shao, L. Zhang, N. Han, Y. Li, Molecular modulation of sequestered copper sites for efficient electroreduction of carbon dioxide to methane, *Adv. Funct. Mater.* 33 (2023) 2214062, <https://doi.org/10.1002/adfm.202214062>.
- [28] K. Chen, M. Cao, Y. Lin, J. Fu, H. Liao, Y. Zhou, H. Li, X. Qiu, J. Hu, X. Zheng, M. Shakouri, Q. Xiao, Y. Hu, J. Li, J. Liu, E. Cortés, M. Liu, Ligand engineering in nickel phthalocyanine to boost the electrocatalytic reduction of CO₂, *Adv. Funct. Mater.* 32 (2022) 2111322, <https://doi.org/10.1002/adfm.202111322>.
- [29] K. Zhang, B. Jin, C. Park, Y. Cho, X. Song, X. Shi, S. Zhang, W. Kim, H. Zeng, J. H. Park, Black phosphorene as a hole extraction layer boosting solar water splitting of oxygen evolution catalysts, *Nat. Commun.* 10 (2019) 2001, <https://doi.org/10.1038/s41467-019-10034-1>.
- [30] S. Yang, Y. Yu, M. Dou, Z. Zhang, F. Wang, Edge-functionalized polyphthalocyanine networks with high oxygen reduction reaction activity, *J. Am. Chem. Soc.* 142 (2020) 17524–17530, <https://doi.org/10.1021/jacs.0c07249>.
- [31] S. Yang, Y. Yu, M. Dou, Z. Zhang, L. Dai, F. Wang, Two-dimensional conjugated aromatic networks as high-site-density and single-atom electrocatalysts for the oxygen reduction reaction, *Angew. Chem. Int. Ed.* 58 (2019) 14724–14730, <https://doi.org/10.1002/ange.201908023>.
- [32] Y. Deng, H. Zhou, Y. Zhao, B. Yang, M. Shi, X. Tao, S. Yang, R. Li, C. Li, Spatial separation of photogenerated charges on well-defined bismuth vanadate square nanocrystals, *Small* 18 (2022) 2103245, <https://doi.org/10.1002/smll.202103245>.
- [33] L. Jiang, M. Gu, S. Zhao, H. Wang, X. Huang, A. Gao, H. Zhu, P. Sun, X. Liu, H. Lin, X. Zhang, Regulating the active sites of metal-phthalocyanine at the molecular level for efficient water electrolysis: double deciphering of electron-withdrawing groups and bimetallic, *Small* 19 (2023) 2207243, <https://doi.org/10.1002/smll.202207243>.
- [34] Y. Song, X. Zhang, Y. Zhang, P. Zhai, Z. Li, D. Jin, J. Cao, C. Wang, B. Zhang, J. Gao, L. Sun, J. Hou, Engineering MoO_x/MXene hole transfer layers for unexpected boosting of photoelectrochemical water oxidation, *Angew. Chem. Int. Ed.* 61 (2022) e202200946, <https://doi.org/10.1002/ange.202200946>.
- [35] J. Sun, J. Bian, J. Li, Z. Zhang, Z. Li, Y. Qu, L. Bai, Z.D. Yang, L. Jing, Efficiently photocatalytic conversion of CO₂ on ultrathin metal phthalocyanine/g-C₃N₄ heterojunctions by promoting charge transfer and CO₂ activation, *Appl. Catal. B-Environ.* 277 (2022) 119199, <https://doi.org/10.1016/j.apcatb.2020.119199>.
- [36] P. Yang, R. Wang, H. Tao, Y. Zhang, M.M. Titirici, X. Wang, Cobalt nitride anchored on nitrogen-rich carbons for efficient carbon dioxide reduction with visible light, *Appl. Catal. B-Environ.* 280 (2021) 119454, <https://doi.org/10.1016/j.apcatb.2020.119454>.
- [37] S. Yin, X. Zhao, E. Jiang, Y. Yan, P. Zhou, P. Huo, Boosting water decomposition by sulfur vacancies for efficient CO₂ photoreduction, *Energy Environ. Sci.* 15 (2022) 1556–1562, <https://doi.org/10.1039/d1ee03764a>.
- [38] S. Si, H. Shou, Y. Mao, X. Bao, G. Zhai, K. Song, Z. Wang, P. Wang, Y. Liu, Z. Zheng, Y. Dai, L. Song, B. Huang, H. Cheng, Low-coordination single Au atoms on ultrathin ZnIn₂S₄ nanosheets for selective photocatalytic CO₂ reduction towards CH₄, *Angew. Chem. Int. Ed.* 61 (2022) e202209446, <https://doi.org/10.1002/anie.202209446>.
- [39] J. Zhou, J. Li, L. Kan, L. Zhang, Q. Huang, Y. Yan, Y. Chen, J. Liu, S. Li, Y. Lan, Linking oxidative and reductive clusters to prepare crystalline porous catalysts for photocatalytic CO₂ reduction with H₂O, *Nat. Commun.* 13 (2022) 4681, <https://doi.org/10.1038/s41467-022-32449-z>.